

## Development of a lensless radiomicroscope for cellular-resolution radionuclide imaging

### Authors:

Justin S. Klein

Department of Radiation Oncology, Stanford University, Stanford, CA 94305, United States of America

Telephone: (650) 736-0619

Fax: 650-723-7254

jstklein@gmail.com

Tae Jin Kim

Department of Radiation Oncology, Stanford University, Stanford, CA 94305, United States of America

Guillem Pratx (Corresponding Author)

Department of Radiation Oncology, Stanford University, Stanford, CA 94305, United States of America

Telephone: (650) 724-9829

Fax: 650-723-7254

pratx@stanford.edu

Word Count: 4939

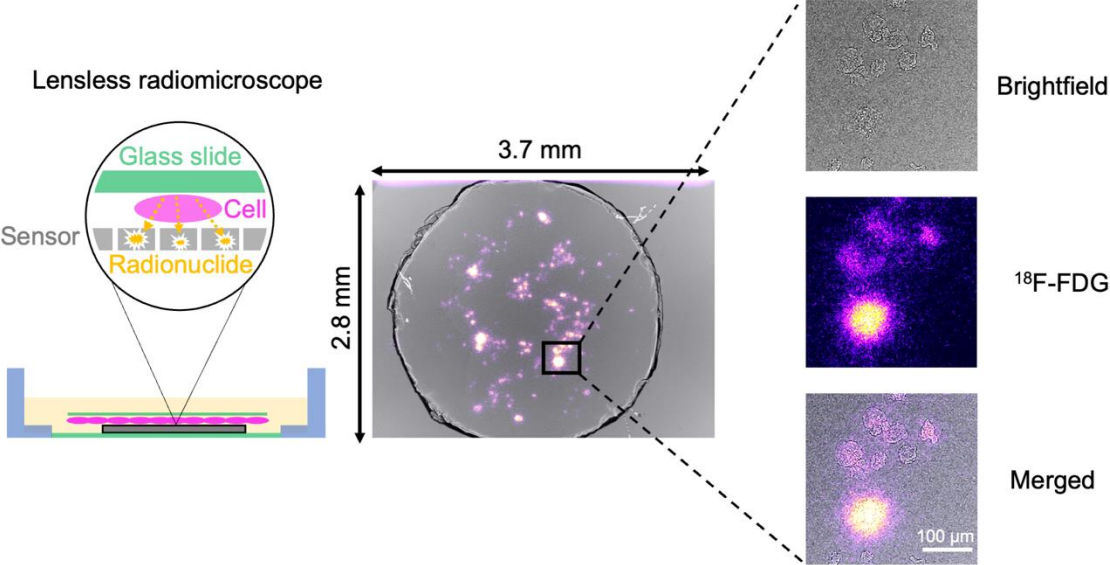
### Disclosures:

Justin Klein was supported by T32CA118681. No potential conflicts of interest relevant to this article exist.

### Short running title:

*In vitro* lensless radiomicroscopy

**GRAPHICAL ABSTRACT**



## ABSTRACT

The action of radiopharmaceuticals takes place at the level of cells. However, existing radionuclide assays can only measure uptake in bulk or in small populations of single cells. This potentially hinders the development of effective radiopharmaceuticals for disease detection, staging, and treatment.

**Methods:** We have developed a new imaging modality, the lensless radiomicroscope (LRM), for *in vitro*, cellular-resolution imaging of beta- and alpha-emitting radionuclides. The palm-sized instrument is constructed from off-the-shelf parts for a total cost of <\$100, about 500× less than the radioluminescence microscope, its closest equivalent. The instrument images radiopharmaceuticals by direct detection of ionizing charged particles via a consumer-grade complementary metal-oxide semiconductor (CMOS) detector. **Results:** The LRM can simultaneously image >5k cells within its 1 cm<sup>2</sup> field-of-view, a 100× increase over state-of-the-art technology. It has spatial resolution of 5 μm for brightfield imaging and 30 μm for <sup>18</sup>F positron imaging. We used the LRM to quantify <sup>18</sup>F-fluorodeoxyglucose (FDG) uptake in MDA-MB-231 breast cancer cells 72 hours after radiation treatment. Cells receiving 3 Gy were 3× larger (mean = 3116 μm<sup>2</sup>) than their untreated counterparts (mean = 940 μm<sup>2</sup>) but had 2× less <sup>18</sup>F-FDG per area (mean = 217 Bq/mm<sup>2</sup>), a finding in agreement with the clinical use of this tracer to monitor response. Additionally, the LRM was used to dynamically image the uptake of <sup>18</sup>F-FDG by live cancer cells, and thus measure their avidity for glucose. **Conclusion:** The LRM is a high-resolution, large field of view, and cost-effective approach to image radiotracer uptake with single-cell resolution *in vitro*.

**Keywords:** radionuclide imaging, *in vitro* assays, <sup>18</sup>F-fluorodeoxyglucose, CMOS detector

## INTRODUCTION

The past decade has witnessed a significant increase in the number of radiopharmaceuticals approved for diagnostic and therapeutic use in humans. To receive such approval, these radiopharmaceuticals have undergone rigorous evaluation and characterization, including preclinical and clinical studies. During the early phase of this process, *in vitro* data are often generated to identify and validate promising leads. In addition, existing radiopharmaceuticals continue to be studied even well after they have been approved for human use (1–3). However, most *in vitro* cell studies are limited in their ability to resolve the action of the radiopharmaceuticals at the level of individual cells. Most existing assays can only measure the aggregated behavior of millions of cells, complicating efforts to study specific cells of interest within heterogenous populations (4).

Radioluminescence microscopy (RLM), a technique for *in vitro* radionuclide imaging, was previously developed to address this need. The method allows dynamic imaging of live cells over a 1 mm<sup>2</sup> field-of-view, equating to ~50 to 100 cells simultaneously. RLM consists of a high sensitivity camera coupled to a microscope objective that images a thin (typically 100-500 μm) scintillator placed above or below a culture monolayer (2). By imaging beta particle scintillation tracks and applying a reconstruction algorithm (5), high-resolution and quantitative measurements of single cells are achievable (6). RLM has been used to study metabolism with <sup>18</sup>F-FDG (7) and cell proliferation with <sup>18</sup>F-fluorothymidine (1) in cell monolayers. The method can also be applied to image 3D -cultured cells including engineered tumor-stroma models (8) and patient-derived tumor organoids (9).

However, the small field-of-view of RLM presents a challenge for biological experiments, requiring repeated acquisitions to attain statistical significance, since it is too small to measure sufficient numbers of cells and collect information on rare cell populations, such as tumor progenitor cells (10).

Additionally, it should be noted that building a RLM and successfully executing experiments requires significant technical skill and, to the best of our knowledge, only a few labs have adopted this technique. The cost of the necessary equipment is also significant, which has hindered dissemination and commercialization of the technique to more sites.

Here, we report the development of a *lensless radiomicroscope* (LRM) for *in vitro*, cellular-resolution radionuclide imaging of large cell populations. Unlike RLM, the LRM uses neither a scintillator nor a microscope objective. Instead, its design is based on the concept of lensless imaging (Figure 1a), which was previously demonstrated for imaging cell samples using cell phone cameras or inexpensive photosensor arrays (11). This new microscope can image brightfield and radionuclide uptake of >5k cells, an 100× increase over RLM, with spatial resolution of 30 μm for radionuclide imaging and 5 μm for brightfield imaging. Additionally, the LRM is a simple and compact device built from inexpensive, readily available consumer electronics. With a total price tag of under \$100 USD, it costs ~500× less than RLM, its predecessor, yet it can acquire radionuclide and brightfield images with similar performance.

To demonstrate the capabilities of this new instrument, we have used the LRM to image the dynamic uptake of <sup>18</sup>F-FDG by MDA-MB-231 breast cancer cells. Additionally, we have demonstrated that it is sensitive to alpha particles, enabling its application for imaging therapeutic radiopharmaceuticals *in vitro*.

## MATERIALS AND METHODS

### Beta Microscope Design

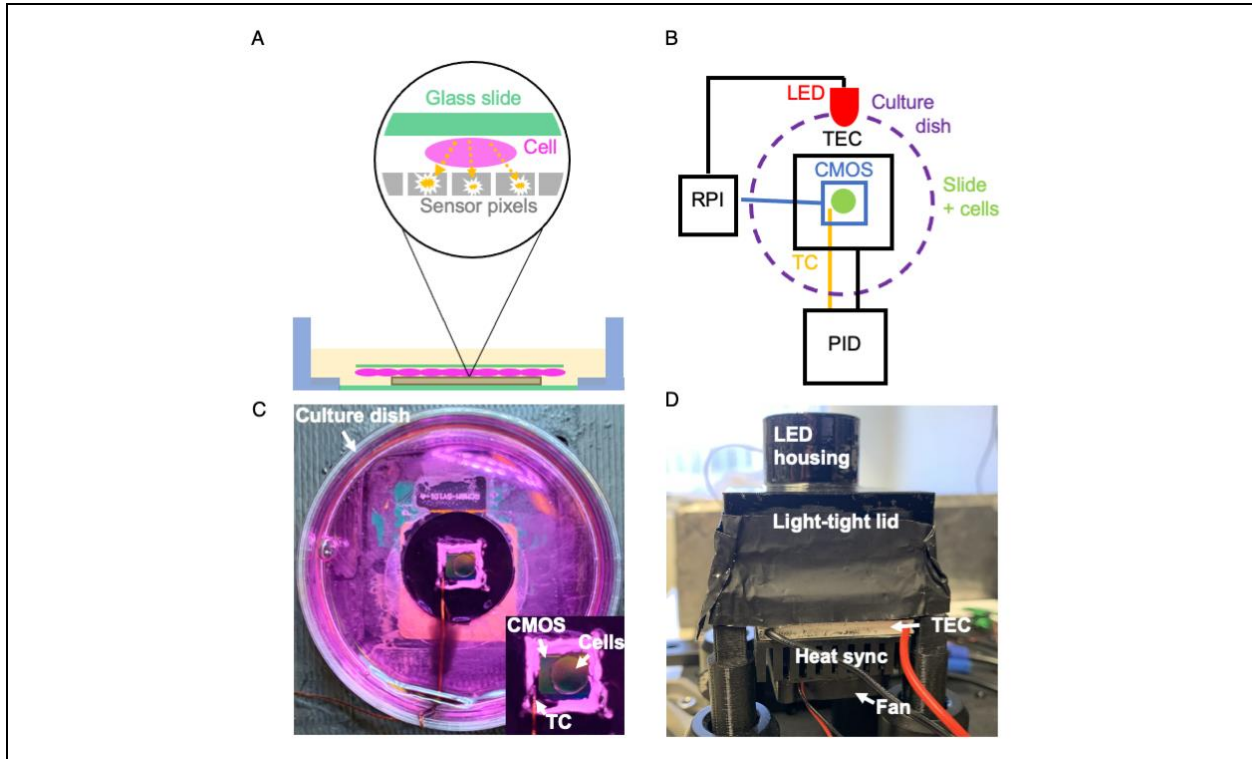


Figure 1: Conceptual, physical, and schematic diagram of the LRM. (A) Cells are grown on a glass slide and treated with alpha- or beta-emitting radiopharmaceuticals. The slide is inverted and placed in direct contact with a CMOS imaging sensor. Emitted particles deposit energy in adjacent CMOS pixels, producing a detectable electronic signal. (B) The LRM consists of an imaging sensor (CMOS) that is read out through a compact Raspberry Pi computer. For live-cell imaging, sensor temperature is regulated by a PID controller (PID) connected to a thermocouple (TC) and thermoelectric cooler (TEC). The computer is also connected to an LED, which can be switched on for brightfield imaging. (C) The beta microscope imaging chamber, filled with media. (D) Light-tight beta microscope enclosure. The LED used for brightfield imaging is housed in the upper cylinder. Attached to the bottom of the enclosure are the thermoelectric cooler, heat sync and fan.

The beta microscope comprises a light-tight imaging chamber with a removable lid made from 3D-printed parts (Figure 1d). Inside the imaging chamber (Figure 1c) is a pixelated Sony IMX219 complementary metal-oxide semiconductor (CMOS) imaging detector (Picamera V2.1, Raspberry Pi Foundation, U.K.) integrated into a 35 mm-diameter cell-imaging dish (Cellvis, Mountain View, CA, USA). The imager has 3280 by 2464 square pixels, each 1.12  $\mu\text{m}$  in size, and a total active area of 3.79 mm by 2.69 mm. The whole imaging dish is easily removable via a J2 FPC connector on the bottom of the dish that mates with the microscope's imaging chamber.

The imaging detector is connected to the camera serial interface of a compact computer (Raspberry Pi Model 3B+, Raspberry Pi Foundation, U.K.). Custom, Python-based software (Python Software Foundation) controls the instrument for brightfield and radionuclide imaging. Microscope software and computer-aided design models are available in our public Git repository: <https://github.com/jstklein/lrm>. Temperature is controlled during cell imaging via a thermoelectric cooler that is coupled to the underside of the PiCamera circuit board. The cooler is controlled by a proportional-integral-derivative (PID) controller that is connected to a thermocouple bonded to the CMOS surface (Figure 1c).

The light-tight enclosure features a 30 mm long tube and aperture-masked red ( $\sim 640$  nm) light-emitting diode (LED) that is driven by a 5 V input/output port on the Raspberry Pi computer through a 1 k $\Omega$  current-limit resistor (Figure 1d). The LED provides semi-collimated light for lensless brightfield imaging. We tested other visible wavelength LEDs (green, white) and found all yielded qualitatively similar results and the red LED was arbitrarily chosen. Given the proximity of the cells to the CMOS sensor, brightfield images can be obtained directly from the sensor without any additional reconstruction.

## Imaging Dish Construction

The lens assembly of the PiCamera was removed and the CMOS detector was carefully extracted from the camera housing. Exposed gold bondwires were protected from the aqueous cell culture environment using a waterproof silicon sealant (Marine Adhesive Sealant 5200FC, 3M, St. Paul, Minnesota, USA). The detector was then glued into the hole at the bottom of the plastic imaging dish using 832HD epoxy (MG Chemicals, Surrey, B.C., Canada). Finally, a glass coverslip was glued behind the detector, sealing the bottom of the imaging chamber.

## Cell Imaging

Cells were grown on glass coverslips that had been prepared for cell culture according to (12) and subsequently treated with fibronectin (Sigma Aldrich, St. Louis, M.O., USA) to improve biocompatibility and facilitate cell attachment. For all imaging experiments, MDA-MB-231 breast cancer cells were grown on round glass cover slips and submerged upside-down into the imaging chamber, in direct contact with the CMOS detector. During imaging, the PID controller is set to hold the temperature of the cells and medium to 37 °C. Without active temperature control, the CMOS imager will exceed physiological temperatures during operation, and potentially interfere with normal cellular processes.

For *static* images, which capture total uptake at a single timepoint, cells were incubated in radiopharmaceutical, washed, and then imaged. For *dynamic* images, which capture the process of radiopharmaceutical transport and accumulation, the radiopharmaceutical was added directly to the imaging chamber and an image time-series was captured immediately thereafter to visualize its uptake.

MDA-MB-231 cells (American Type Culture Collection) were cultured in Dulbecco's Modified Eagle Medium (DMEM) (Thermo Fisher Scientific, cat. no. 11995-065) supplemented with 10% fetal bovine serum 10% FBS (Atlas Biologicals, cat. no. F-0500-A) and 1% penicillin/streptomycin (Thermo Fisher Scientific, cat. no. 15140122) and incubated at 37 °C in a 5% CO<sub>2</sub> environment.

Brightfield images were acquired using autoexposure mode at the maximum resolution of 3280 by 2464 pixels. Raw RGB images were converted to grayscale and stored as 16-bit JPEG2000 images.

To demonstrate the ability of the microscope to image cell staining, some MDA-MB-231 cells were additionally fixed and stained with crystal violet, by first rinsing with PBS, then incubating in 5% w/w crystal violet in 6% v/v glutaraldehyde (Sigma-Aldrich, St. Louis Missouri), and finally rinsed with tap water.

Beta and alpha images were acquired with the following settings: 3280 by 2464 pixels, 10 second exposure duration and analog gain of 2.5. A lower threshold of 3 camera counts was applied to each 10 second exposure to remove camera noise. Multiple thresholded exposures were summed together in memory to produce output images with effective integration times ranging from ~1 to 10 minutes, depending on the experiment. No other image processing or filtering was performed. Image data were stored as a lossless lz4-compressed 16-bit image matrix. Image data and metadata were combined into a Python data structure, serialized using the Python Pickle format, then saved to file.

### **Alpha Imaging**

Alpha emission from a 370 Bq <sup>210</sup>Po needle source (United Nuclear Scientific LLC, Klamath Falls, Oregon, US) was imaged by placing the active tip directly on the microscope's CMOS surface. Three 5-

minute alpha-images were recorded and summed together. A brightfield image of the needle source was also recorded.

### **Physical Characterization**

Beta imaging resolution was assessed by applying the Fourier ring correlation method (13) to a representative image of  $^{18}\text{F}$ -FDG uptake by cancer cells. Briefly, two images of the same cell population were generated, each constructed from half of the acquired frames. The method estimates the cross-correlation between the two images in the spatial frequency domain along concentric rings. A deterministic threshold of 1/7 is then used to yield a quantitative estimate of the spatial resolution of the imager.

In addition, brightfield resolution was characterized by imaging 1  $\mu\text{m}$  amine modified monodispersed superparamagnetic beads (MonoMag Amine Beads, Ocean NanoTech, San Diego, CA, USA). The beads were diluted in ethanol and dried onto the surface of a glass microscope coverslip that was imaged using the brightfield mode of the beta microscope. Resolution was measured from the full width at half maximum of a line profile drawn across a single bead in the brightfield image.

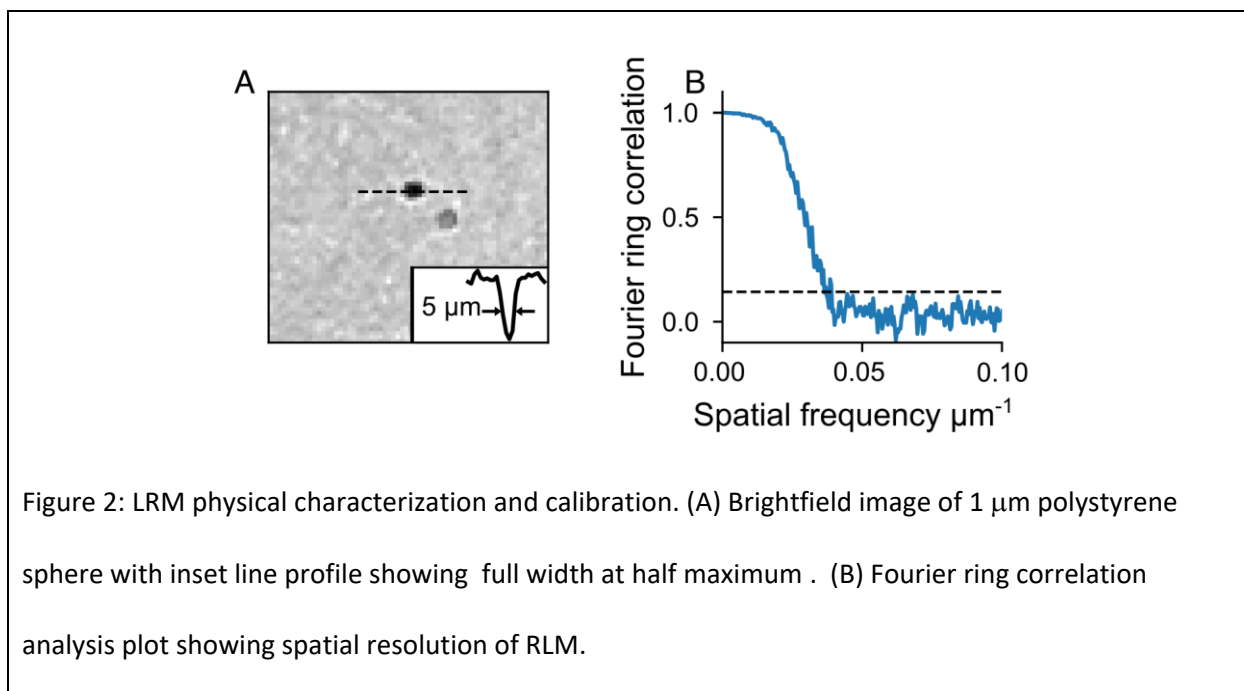
### **Camera Calibration**

A flatfield image was captured by illuminating the imaging sensor with uniform white light. This image was used to compute a per-pixel correction factor that was applied to images generated by the instrument. This correction factor accounts for any non-uniformities in the imaging sensor and lens-related calibration factors built into the proprietary camera firmware.

A calibration factor to convert camera units into  $^{18}\text{F}$  activity was determined as follows. A drop of  $^{18}\text{F}$ -FDG was dried on a glass slide and activity was measured in a dose calibrator to be 108 kBq. The slide was imaged 397 minutes ( $\sim 3.6$  half lives) later using the beta microscope, after it had decayed to 8.9 kBq. This low activity level was used to prevent camera saturation. A region of interest (ROI) was measured around the dried  $^{18}\text{F}$ -FDG droplet. The camera calibration factor was computed as: ROI counts (camera units)  $\times$  Pixel area ( $\text{mm}^2/\text{px}$ ) / ROI activity (Bq)  $\times$  Total imaging time (s), where pixel area =  $1.25 \times 10^{-6} \text{ mm}^2/\text{px}$  (based on CMOS pixel pitch).

## RESULTS

### Characterization



Supplemental Figure 1 shows a time-integrated beta microscope image of a dried 8.9 kBq  $^{18}\text{F}$ -FDG droplet on a glass slide. The final camera calibration factor was computed using *Equation 1* and average measurements from three independent, 50 second beta images. The measurements were: ROI counts = 422,845,211, ROI activity = 8.9 kBq, and total imaging time = 50 s. The final calibration factor

was  $840 \frac{\text{camera units} \times \text{mm}^2}{\text{Bq} \times \text{s} \times \text{px}}$ . When divided into  $^{18}\text{F}$  beta images on a per-pixel basis, the calibration factor yields quantitative images in units of  $\text{Bq}/\text{mm}^2$ .

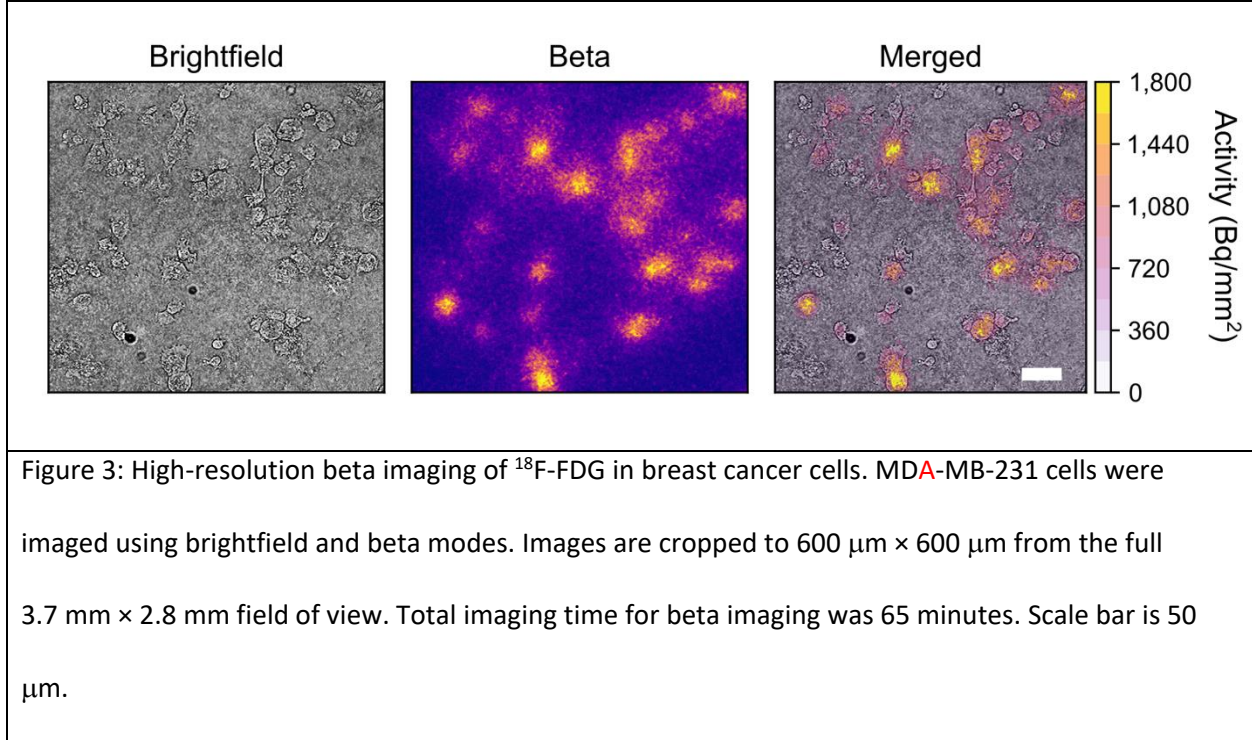
Brightfield resolution was  $5.1 \mu\text{m}$ , based on the full width at half maximum of a  $1 \mu\text{m}$  polystyrene sphere (Figure 2a). The Inset image shows line profile drawn across the sphere (dashed blacked line) and arrows show full width at half maximum. Beta resolution was  $30 \mu\text{m}$ , based on Fourier ring correlation analysis of  $^{18}\text{F}$ -FDG beta images of MDA-MB-231 cells (Figure 2b). This resolution is equivalent to that of RLM and largely determined by the source-detector distance and the physics of positron transport (6).

### **Brightfield Imaging**

To demonstrate the timelapse capabilities of the LRM and the ability of cells to remain viable over prolonged imaging experiments, MDA-MB-231 cells were grown on a glass slide, then imaged in brightfield mode every 5 minutes, for 10 hours (Supplemental Figure 2a). Cell migration could be readily observed in a recorded video of the acquisition (Supplemental Video 1), and no adverse effects were detected.

Additionally, the microscope is capable of imaging fixed and stained cells. Supplemental Figure 2b shows enlarged senescent MDA-MB-231 cells after irradiation with 8 Gy (225 kVp X-ray) and subsequent fixing and staining with crystal violet in glutaraldehyde. The use of a stain induces a visible darkening of the cells in the brightfield images.

### <sup>18</sup>F-FDG Beta Microscope Imaging



We first demonstrate the LRM technique by imaging <sup>18</sup>F-FDG uptake in MDA-MB-231 breast cancer cells (Figure 3). The beta image is the sum of 13 images, each acquired as a 5 min exposure (65 minutes total imaging time). The merged image shows that <sup>18</sup>F-FDG uptake can be localized to individual cells and matches the brightfield image. Due to the proximity of the cells to the detector, the outline of the cells is clearly resolved, with only overlap between adjacent cells. About 50 cells are shown in the cropped field of view and range in activity from 0 Bq/mm<sup>2</sup> up to 1800 Bq/mm<sup>2</sup>, indicating a wide range of metabolic activity in this population. Healthier-looking cells (larger, attached, dividing) appear to be more metabolically active than unhealthy ones (detached, granular, shriveled). The images also confirm that background signal is very low in areas where cells are not present, even for extended imaging experiments.

## $^{18}\text{F}$ -FDG Imaging of Radiation Treated Breast Cancer Cells

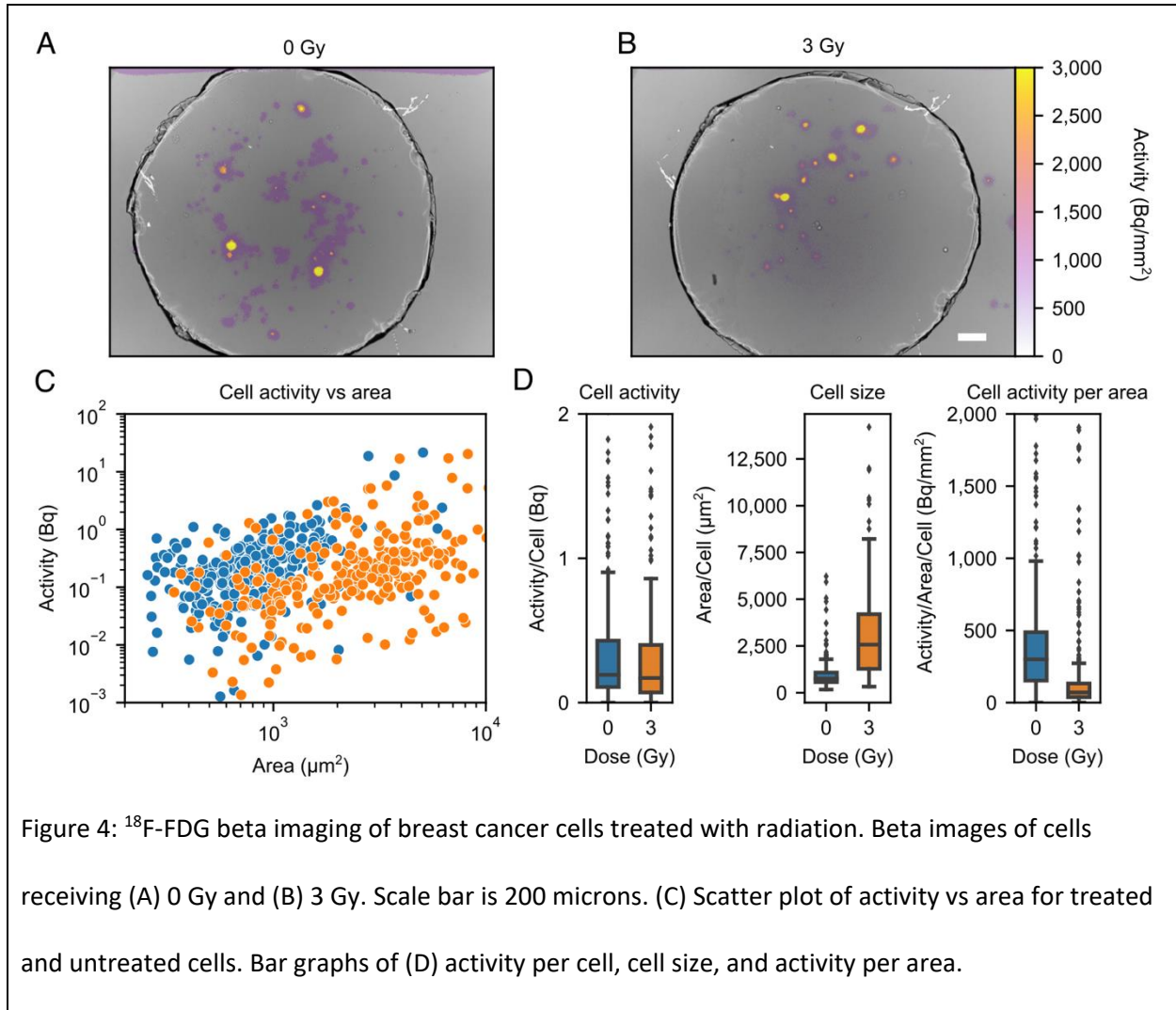


Figure 4:  $^{18}\text{F}$ -FDG beta imaging of breast cancer cells treated with radiation. Beta images of cells receiving (A) 0 Gy and (B) 3 Gy. Scale bar is 200 microns. (C) Scatter plot of activity vs area for treated and untreated cells. Bar graphs of (D) activity per cell, cell size, and activity per area.

Figure 4 demonstrates that LRM can be used to determine the response of MDA-MB-231 cells to radiation therapy on the basis of  $^{18}\text{F}$ -FDG uptake. Cells were irradiated with 0 Gy and 3 Gy of 225 kVp X-ray three days prior to image acquisition using the LRM.

To quantify the images, ROIs were drawn around cells, and area and activity were measured.

Figure 4c shows activity vs area for all cells in the experiment. Data represent ROIs measured from four

beta images with total integration times of 75 minutes (0 Gy experiment) and 45, 60, or 105 minutes (3 Gy experiment).

Figure 4d shows aggregated measurements from cell ROIs. Cells receiving 0 Gy ( $n = 301$ ) had significantly smaller area (mean =  $940 \mu\text{m}^2$ ) but overall greater activity per area (mean =  $445 \text{Bq}/\text{mm}^2$ ). Cells receiving 3 Gy ( $n = 260$ ) had larger area (mean =  $3116 \mu\text{m}^2$ ), but less activity per area (mean =  $217 \text{Bq}/\text{mm}^2$ ). All results were statistically significant ( $P < 0.01$ ) per Welch's T-test. Both groups had similar activity per cell (0 Gy mean =  $0.50 \text{Bq}$ ; 3 Gy mean =  $0.67 \text{Bq}$ ;  $P > 0.01$ ).

#### Dynamic $^{18}\text{F}$ -FDG Beta Microscope Imaging

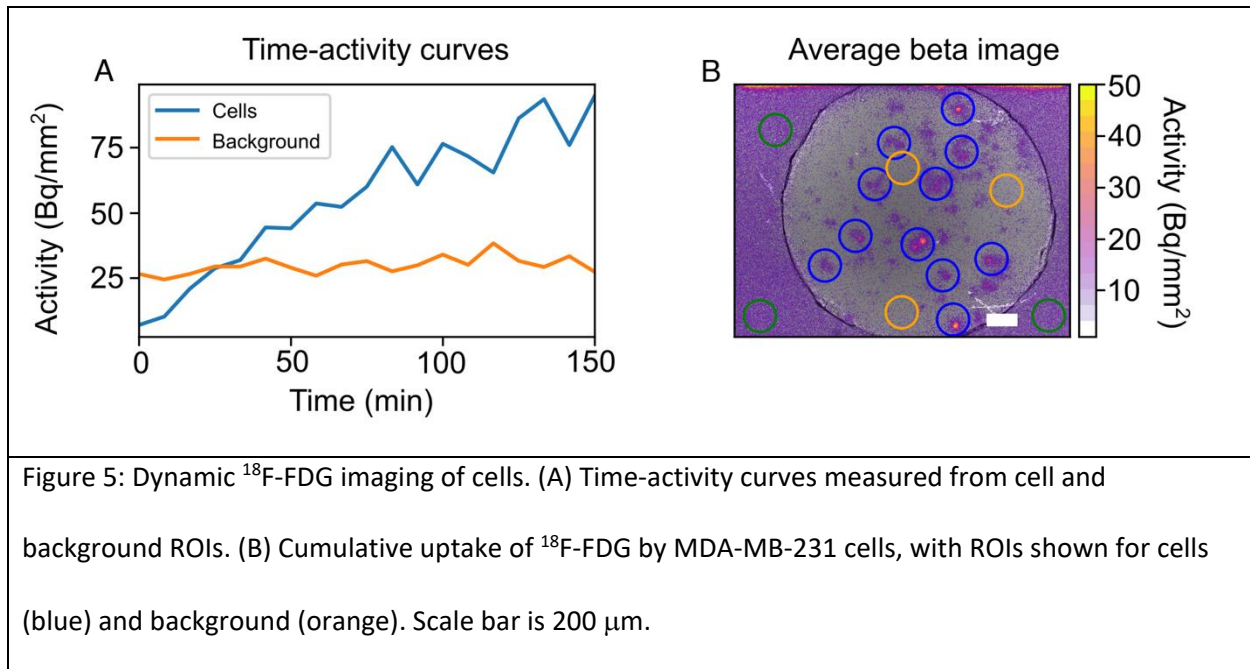
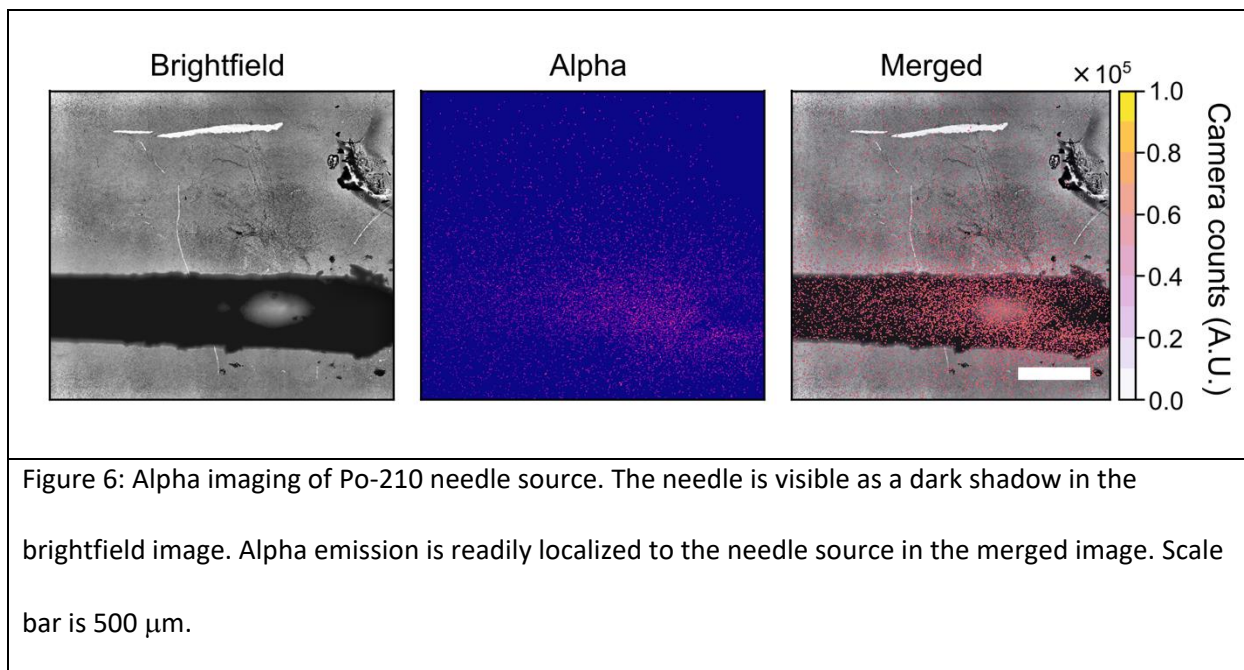


Figure 5 demonstrates dynamic imaging of  $^{18}\text{F}$ -FDG uptake by MDA-MB-231 cells over a 190 min period. LRM images were acquired every 10 min, resulting in 19 frames, and the corresponding time-activity curves were computed based on user-defined circular ROIs (Figure 5b). For this study, 5 MBq/ml of  $^{18}\text{F}$ -FDG in DMEM was added to the imaging chamber immediately prior to imaging the dynamic uptake of the tracer by the cells. The average  $^{18}\text{F}$ -FDG distribution over the entire study period is shown in Figure 5b, along with the ROIs that were used. The time activity curves for the cells were corrected by subtracting the background signal.

The beta image is merged with the grayscale brightfield image and ROIs have been drawn over clusters of cells (blue) and empty background regions (orange). The image shows regions of significant focal uptake, corresponding to dense clusters of cells. Background signal is significantly lower under the cover glass compared to outside due to lower volume and shielding by the cover glass.

Time-activity curves of cell and background ROIs (Figure 5a) show  $^{18}\text{F}$ -FDG uptake as a function of time. These curves have been corrected for radioactive decay and drift in detector gain by normalizing them using the background signal outside the circular cover glass region. A movie of  $^{18}\text{F}$ -FDG uptake has been included as Supplemental [Video 2](#).



### Alpha Particle Imaging

Figure 6 shows alpha and brightfield images of a  $^{210}\text{Po}$  needle source. The needle appears as a long dark shadow in the brightfield image. The alpha image is the sum of three 5-minute acquisitions. Compared to beta particles, alpha particles produce an intense and focal signal on the detector. The merged image shows that the alpha signal is readily localized to the needle source.

### DISCUSSION

This study presents a novel lensless radiomicroscope that can image commonly used radiotracers at single-cell resolution in 2D cell cultures. The instrument is compact and inexpensive, yet it can image samples with  $>1\text{ cm}^2$  field of view and  $30\ \mu\text{m}$  spatial resolution. The microscope is capable of prolonged, timelapse brightfield *in vitro* imaging of stained or unstained cells (Supplemental Figure 2, Supplemental Video 1), and beta (Figures 3, 4 and 5) or alpha (Figure 6) imaging.

Compared to other solid-state radiation detectors, such as for instance a position-sensitive avalanche photodiode (14), a lensless CMOS detector can also be used for imaging cells in brightfield mode, providing images of both the cells and the distribution of the radiotracer. These capabilities could potentially be embedded within microfluidics devices for in vitro radiobiological assays (13) or for quality control of radiotracer production (15). Additionally, the system is built from inexpensive consumer-grade components, including a Raspberry Pi minicomputer (\$35), a CMOS camera (\$25), a Pelletier cooling system (\$35), and a 3D printed housing (<\$10). The system is therefore highly cost-effective compared to other previously developed imaging methods.

Figure 3 reveals static  $^{18}\text{F}$ -FDG beta images of MDA-MB-231 cells and shows that the beta signal is easily localized to individual cells. The spatial resolution of  $^{18}\text{F}$  images is estimated to be 30  $\mu\text{m}$ , based on Fourier ring correlation analysis of the LRM images, which is sufficient in most cases to distinguish individual cells. This estimate, which is obtained through a computational method, is consistent with fact that, in Figure 3, adjacent cells can be readily resolved. Spatial resolution for beta imaging is primarily determined by the physical travel of the positrons before reaching the sensor, regardless of the type and pixel size of the sensor used to detect the ionizing radiation. Thus, although the pixels are very small, the spatial resolution of the LRM is similar to that of other methods that rely on larger pixels, such as RLM (6). The use of CMOS devices with larger pixels could potentially allow improved signal-to-noise with no loss of resolution, however, the trend in consumer camera electronics is towards smaller form factors and pixels. Additionally, once calibrated, the LRM can be used to provide quantitative estimates of radioactivity distribution in cells. The calibration factor we have provided is relevant only for  $^{18}\text{F}$  and the calibration procedure would have to be repeated if other isotopes were imaged.

To illustrate the capabilities of the microscope, we measured  $^{18}\text{F}$ -FDG uptake in cells irradiated with 0 Gy or 3 Gy of X-rays (Figure 4). Radiation is often used as a treatment for solid tumors, with nearly 50% of all cancer patients receiving some form of radiation for their disease. FDG-PET is a common readout of treatment response, but the significance of the PET measurement is unclear because irradiated cells may remain metabolically active, even if they can no longer replicate. To investigate this question, measurements from more than 500 cells were made using the beta microscope in a single experiment. Three days after receiving 3 Gy of X-ray radiation, cells were on average three times larger (mean area =  $3116 \mu\text{m}^2$ ) than their untreated counterparts but had half as much  $^{18}\text{F}$ -FDG per area. The brightfield images also revealed that the 3 Gy-treated cells had enlarged nuclei, a common occurrence in radiation-treated cells that is due to the failure of these cells to advance through mitosis. The decreased  $^{18}\text{F}$ -FDG concentration inside the cells suggests decreased metabolic activity, likely due to radiation-induced damage of the cell's metabolic machinery. Of note, previous studies noted that cells that survived irradiation actually had higher  $^{18}\text{F}$ -FDG uptake than control non-irradiated cells (16,17), based on bulk gamma counting measurements normalized by the number of viable cells. Our study found no substantial difference in uptake between non-irradiated and irradiated, but the difference may be due to the timing and methodology employed for measuring this quantity.

Additionally, we demonstrated the feasibility of dynamic  $^{18}\text{F}$ -FDG studies using the instrument (Figure 6). Dynamic images were acquired every 10 min to yield aggregated time-activity curves that represent the active transport of the tracer by the cells. After decay correction, the measured background due to free  $^{18}\text{F}$ -FDG in the culture medium was found to be constant over the course of the experiment. In contrast, the radioactive signal measured at the location of MDA-MB-231 cells rose over time at a nearly constant rate over the 2-hour duration of the experiment. The imaged cells did not have

initially any detectable radioactivity, but by the end of the experiment, they achieved radiotracer uptake equal to about 6X the background concentration.

Finally, using a sealed  $^{210}\text{Po}$  source, we demonstrated the ability of the LRM to image alpha particles. This capability opens the door for imaging therapeutic alpha-emitting radionuclides, which are an important new class of therapy. The LRM in this context could be used to investigate the distribution of these agents at the level of individual cells in heterogeneous populations of cells and prevent the emergence of resistant subclones.

It should be noted that despite the impressive performance of this instrument, only minimal optimizations for image quality and sensitivity have been made thus far. There are likely significant gains to be had with further software optimization, alone. For example, in previous work, we found that signal-to-noise ratio could be significantly improved by processing the images in pulse-counting mode rather than integration mode (5). Similarly, the CMOS-based LRM could acquire large numbers of frames with short exposures to enumerate individual decay events.

While the pixelated CMOS sensor provides many advantages for this application, a few limitations of the method should be highlighted. First, the 10 bit A/D converter limits the maximum signal to 1024 camera units per pixel per frame. At a readout speed of 1 Hz, with  $^{18}\text{F}$ , this would limit the maximum detectable activity to 10.8 Bq/px. Additionally, another limitation is that, unlike the previously developed RLM, the LRM lacks fluorescence capabilities. This capability could likely be enabled through harnessing built-in Bayer array or coating the CMOS pixels with a bandpass filter to obtain fluorescence images of cells in a lensless manner (18).

Finally, though we were able to reuse the same CMOS detector for many experiments, we expect that it will eventually degrade due to radiation damage. Given its relatively low cost, it is a consumable component of the microscope that can be regularly replaced.

## **CONCLUSION**

The experiments shown here are a proof-of-concept for the LRM, a new imaging instrument capable of *in vitro* high-resolution imaging of beta- and alpha-emitting radionuclides. This instrument is simpler and far less costly than current technology while offering an unprecedentedly large 1 cm<sup>2</sup> field-of-view and 30 μm resolution. Our results demonstrate a variety of potential workflows that could foreseeably be used for radiopharmaceutical development, quality control, and cancer biology investigations. Because the LRM is low cost and constructed from readily available components, we anticipate that this new technology will make *in vitro* single-cell radionuclide imaging more accessible and enable new investigations in the biological realm.

## **KEY POINTS**

QUESTION: Can a low cost lensless radiomicroscope visualize cellular-level uptake of radionuclides?

PERTINENT FINDINGS: We have developed a low-cost imaging modality for *in vitro* imaging of alpha and beta-emitting radionuclides and imaged quantitative changes in cellular <sup>18</sup>F<sup>18</sup>FDG uptake after radiation treatment.

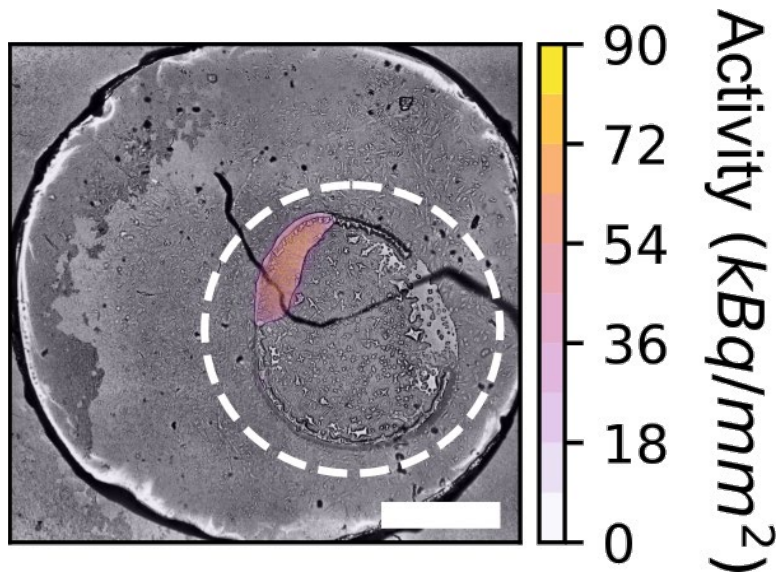
IMPLICATIONS FOR PATIENT CARE: The lensless radiomicroscope will aid in the development of effective radiopharmaceuticals by allowing study of their action at the cellular level.

## REFERENCES

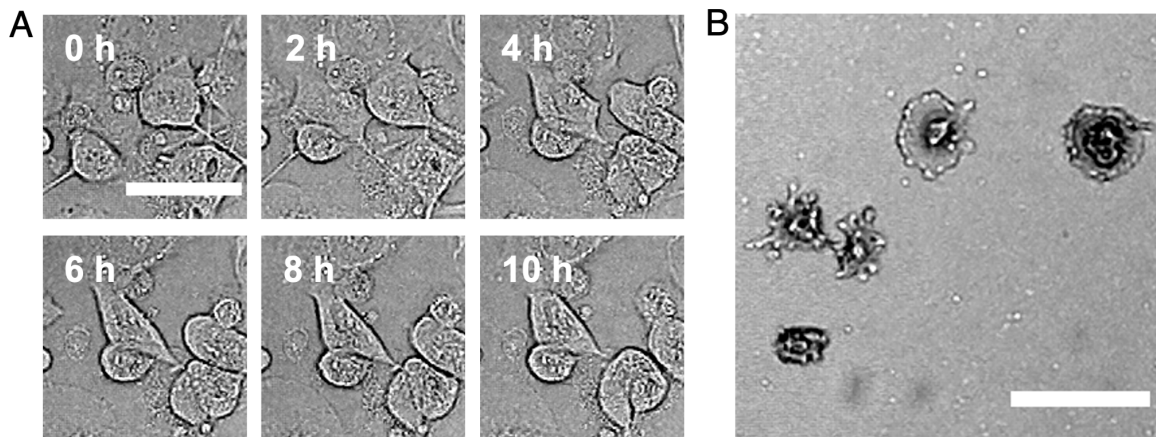
1. Sengupta D, Pratz G. Single-cell characterization of FLT uptake with radioluminescence microscopy. *J Nucl Med*. 2016;57:1136-1140.
2. Kim TJ, Türkcan S, Pratz G. Modular low-light microscope for imaging cellular bioluminescence and radioluminescence. *Nat Protoc*. 2017;12:1055-1076.
3. Liu Z, Lan X. Microfluidic radiobioassays: a radiometric detection tool for understanding cellular physiology and pharmacokinetics. *Lab Chip*. 2019;19:2315-2339.
4. Cherry SR, Sorenson JA, Phelps ME. Physics in nuclear medicine. Elsevier Health Sciences; 2012.
5. Pratz G, Chen K, Sun C, et al. High-resolution radioluminescence microscopy of  $^{18}\text{F}$ -FDG uptake by reconstructing the  $\beta$ -Ionization track. *J Nucl Med*. 2013;54:1841-1846.
6. Wang Q, Sengupta D, Kim TJ, Pratz G. Performance evaluation of  $^{18}\text{F}$  radioluminescence microscopy using computational simulation. *Med Phys*. 2017;44:1782-1795.
7. Pratz G, Chen K, Sun C, et al. Radioluminescence microscopy: measuring the heterogeneous uptake of radiotracers in single living cells. *PLOS ONE*. 2012;7(10): e46285.
8. Khan S, Kim S, Yang YP, Pratz G. High-resolution radioluminescence microscopy of FDG uptake in an engineered 3D tumor-stoma model. *Eur J Nucl Med Mol Imaging*. 2021; 48(11):3400-3407.
9. Khan S, Shin JH, Ferri V, et al. High-resolution positron emission microscopy of patient-derived tumor organoids. *Nat Commun*. 2021;12(1):5883.
10. Reya T, Morrison SJ, Clarke MF, Weissman IL. Stem cells, cancer, and cancer stem cells. *Nature*. 2001;414:105-111.
11. Ozcan A, McLeod E. Lensless imaging and sensing. *Annu Rev Biomed Eng*. 2016;18:77-102.
12. Fischer AH, Jacobson KA, Rose J, Zeller R. Preparation of slides and coverslips for microscopy. *Cold Spring Harb Protoc*. 2008;2008(5):pdb.prot4988 .
13. Kim TJ, Ha B, Bick AD, Kim M, Tang SKY, Pratz G. Microfluidics-coupled radioluminescence microscopy for in vitro radiotracer kinetic studies. *Anal Chem*. 2021;93:4425-4433.
14. Vu NT, Yu ZTF, Comin-Anduix B, et al. A beta-camera integrated with a microfluidic chip for radioassays based on real-time imaging of glycolysis in small cell populations. *J Nucl Med Off Publ Soc Nucl Med*. 2011;52:815-821.
15. Ha NS, Sadeghi S, van Dam RM. Recent progress toward microfluidic quality control testing of radiopharmaceuticals. *Micromachines*. 2017;8:337.

16. Higashi K, Clavo AC, Wahl RL. In Vitro Assessment of 2-fluoro-2-deoxy-D glucose, L-methionine and thymidine as agents to monitor the early response of a human adenocarcinoma cell line to radiotherapy. *J Nucl Med.* 1993;34:773-779.
17. Senekowitsch-Schmidtke R, Matzen K, Truckenbrodt R, Mattes J, Heiss P, Schwaiger M. Tumor cell spheroids as a model for evaluation of metabolic changes after irradiation. *J Nucl Med.* 1998;39:1762-1768.
18. Kim M, Pan M, Gai Y, et al. Optofluidic ultrahigh-throughput detection of fluorescent drops. *Lab Chip.* 2015;15:1417-1423.

Supplemental Figures and Videos



Supplemental Figure 1: Merged brightfield/beta image of a dried  $^{18}\text{F}$ -FDG drop. Scale bar is 500 microns.



Supplemental Figure 2: Brightfield imaging of live and fixed cells. (A) Time lapse brightfield images of MDA-MB-231 cells up to 10 hours. Scale bar is 50  $\mu\text{m}$ . (B) Irradiated MDA-MB-231 cells (8 Gy dose), fixed and stained with crystal violet blue. Scale bar is 100  $\mu\text{m}$ .

Supplemental Video 1: Time-lapse brightfield movie of MDA-MB231 cells. Cells were imaged every 5 min for a total of 10 hours. Movie represents 462  $\mu\text{m}$  by 462  $\mu\text{m}$  subset of field-of-view. Scale bar is 100  $\mu\text{m}$ .

Supplemental Video 2: Decay-corrected kinetic  $^{18}\text{F}$ FDG LRM movie of MDA-MB231 cells. Cells were incubated with 5 MBq/mL  $^{18}\text{F}$ FDG and imaged immediately. Each frame is 10 minutes of beta signal integration time. Total imaging time is 190 minutes. Movie represents 462  $\mu\text{m}$  by 462  $\mu\text{m}$  subset of field-of-view. Scale bar is 100  $\mu\text{m}$ .